HHS Public Access

Author manuscript

J Magn Reson Imaging. Author manuscript; available in PMC 2020 January 01.

Published in final edited form as:

J Magn Reson Imaging. 2019 January ; 49(1): 141–151. doi:10.1002/jmri.26219.

Effect of microscopic susceptibility gradients on chemical-shift based fat fraction quantification in supraclavicular fat

Drew McCallister, BS[1,3], **Le Zhang, PhD**[2,3], **Alex Burant, MS**[1,3], **Laurence Katz, MD**[4], and **Rosa Tamara Branca, PhD**[1,3,*]

[1]Department of Physics and Astronomy, University of North Carolina at Chapel Hill, US

[2]Department of Applied Physical Science, University of North Carolina at Chapel Hill, US

[3]Biomedical Research Imaging Center, University of North Carolina at Chapel Hill, US

[4]Department of Emergency Medicine, University of North Carolina at Chapel Hill, US

Abstract

Background—Susceptibility differences between fat and water can cause changes in the water-fat frequency separation that can negatively affect the accuracy of fat fraction techniques. This may be especially relevant for brown adipose tissue as MRI fat fraction techniques have been proposed for its detection.

Purpose—To assess the effect of microscopic magnetic susceptibility gradients on the water-fat frequency separation and its impact on chemical-shift based fat fraction quantification techniques in the supraclavicular fat, where brown adipose tissue is commonly found in humans.

Study Type—Prospective

Population/Subjects/Phantom/Specimen/Animal Model—Subjects: eleven healthy volunteers, mean age of 26 and mean BMI of 23, three overweight volunteers, mean age of 38 and mean BMI of 33. Phantoms: bovine phantom and intralipid fat emulsion. Simulations: various water-fat distributions.

Field Strength/Sequence—6-echo gradient echo chemical-shift-encoded sequence at 3T

Assessment—Fat fraction values as obtained from a water-fat spectral model accounting for susceptibility-induced water-fat frequency variations were directly compared to traditional spectral models which assume constant water-fat frequency separation.

Statistical Tests—Two-tail t-tests were used for significance testing($P<0.05$.) A BIC difference of 6 between fits was taken as strong evidence of an improved model.

Results—Phantom experiments and simulation results showed variations of the water-fat frequency separation up to 0.4 ppm and 0.6 ppm, respectively. In the supraclavicular area, the water-fat frequency separation produced by magnetic susceptibility gradients varied by as much as

*Correspondence to: Rosa Tamara Branca, Ph.D.: Department of Physics and Astronomy, University of North Carolina at Chapel Hill, Chapel Hill, NC 27599, USA. rtbranca@unc.edu.

±0.4 ppm, with a mean of 0.08±0.14 ppm, producing a mean difference in fat fraction of −1.26±5.26%.

Conclusions—In the supraclavicular fat depot, microscopic susceptibility gradients that exist within a voxel between water and fat compartments can produce variations in the water-fat frequency separation. These variations may produce fat fraction quantification errors of 5% when a spectral model with a fixed water-fat frequency separation is applied, which could impact MR brown fat techniques.

Keywords

Brown Adipose Tissue; Imaging; Fat Fraction; Magnetic Susceptibility; Chemical shift encoding; Spectra

Introduction

Since its rediscovery in adult humans, brown adipose tissue (BAT) has become the subject of considerable research(1). This tissue is dedicated to non-shivering thermogenesis, a mechanism by which intracellular triglycerides are first hydrolyzed and then oxidized in the mitochondria of brown adipocytes for heat production. As such, stimulation of non-shivering thermogenesis by BAT has been proposed to reduce adiposity in adult humans(2–4).

In adult humans, where this tissue is present only in scattered amounts around major blood vessels, muscle, or mixed within the more abundant white fat, detection of BAT is still a challenge(5,6). For BAT detection, fat faction MRI techniques have been proposed(7). These techniques take advantage of the differences in hydration between brown adipose tissue and white adipose tissue (WAT)(8). However, direct comparison of BAT maps obtained by MR fat fraction techniques with ^{18}F-FDG-PET BAT maps have shown that, unlike in mice, the range of BAT fat fractions in adult humans is large enough that tissue hydration alone is not a reliable marker for the differentiation of BAT from WAT(9,10). In principle, to increase detection specificity, one could measure BAT lipid consumption during stimulation of non shivering thermogenesis by cold exposure(11–13). However, because changes in tissue fat fraction due to fat oxidation in BAT are typically small(8,12), errors in fat fraction quantification could easily overshadow these changes.

MR fat fraction (FF) quantification in humans was originally proposed and developed in large part to replace non-targeted tissue biopsy for the detection of liver steatosis(14,15). For this purpose, chemical-shift encoded acquisitions (CSE) have been developed(16,17), where the signal from multiple echoes is acquired and then fit to a specific water-fat spectral model. To reduce errors and biases in FF quantification, CSE multi-echo methods also account for differences in T2* of water and fat spins, as well as for macroscopic field inhomogeneities(18,19). Also, 6,7, and 9-peak fat spectral models are most commonly used in CSE reconstruction protocols, with no specific choice having currently been proven to be superior to the rest, but showing significant improvement over the single peak fat spectral model(20). In these experiments, the relative intensity and frequency separation between the different lipid protons and the relative separation between water and lipid protons is either set using spectra from previous studies, or calibrated in a pre-scan protocol(14,20–22).

Although the frequency separation between the different lipid protons is expected not to vary notably, the water-fat frequency separation is however sensitive to a number of factors such as temperature and magnetic susceptibility gradients(23). The effect of temperature, which is known to reduce the water-fat separation by 0.01ppm/°C, on CSE fat quantification protocols was recently investigated by Hernando et al(24). Authors showed that even a temperature variation of 10°C, that is expected to produce a water-fat frequency shift of just 0.1ppm, could lead to large FF quantification errors, on the order of 5% or higher. Earlier, Karampinos et al. (25) investigated the effect of microscopic susceptibility gradients in the context of fat infiltration in muscle. Unlike macroscopic field inhomogeneities, which shift water and fat spins within a voxel by the same amount and in the same direction, microscopic susceptibility gradients, originating from the specific intra-voxel distribution of water and fat spins, can shift water and fat spins by different amounts. As a result, the water-fat frequency separation for non-homogenous samples is expected to vary.

To this end, Karampinos et al. showed that, while the assumption of a single spectra has been shown to be a reasonable assumption for the liver(26), for the specific case of quantification of fat infiltration in skeletal muscle, magnetic susceptibility gradients could cause errors. Specifically, by modeling fat infiltrated into skeletal muscle as an infinite cylinder of fat in water, depending on the relative orientation of this infinite cylinder with respect to the direction of the main magnetic field, they estimated a variation in the water-fat frequency separation as large as 0.2 ppm. To account for this susceptibility-induced shift in the water-fat separation, they proposed the inclusion of a variable water-fat frequency shift in their spectral model(25). To this end, the scope of this work was to analyze how the accuracy of fat fraction MR techniques in supraclavicular fat is affected by microscopic susceptibility gradients present in this region with specific attention to the detection of BAT.

Methods

Fat Fraction CSE algorithms

While macroscopic magnetic field gradients produce a frequency shift of the entire 1H spectrum, microscopic susceptibility gradients generated at water-fat interfaces generally shift water and fat spins by different amounts. In order to quantify these susceptibility-induced shifts and assess their effect on the accuracy of CSE FF quantification methods, two magnitude-based reconstruction algorithms were used. Unlike complex fitting algorithms, which employ a signal model with an overall phase term that accounts for macroscopic field inhomogeneities, magnitude-based reconstruction algorithms do not require fitting of the phase shift from macroscopic field inhomogeneities. Thus, the use of magnitude-based reconstruction algorithms allow for the independent assessment of the effect of microscopic inhomogeneities generated by susceptibility gradients.

The first algorithm (fixed spectral model) used was the standard magnitude-based CSE algorithm, employing the following signal model

$$|S_n| = |(M_w + C_n M_f) e^{-R^*_{2eff} TE_n}| \quad [1]$$

where C_n is a known complex coefficient describing the contribution to the fat signal from multiple fat components:

$$C_n = \sum_{i=1}^{7} w_i e^{j(2\pi\Delta f_i TE_n)} \quad [2]$$

A seven-peak fat spectral model with well defined w_i and Δf_i values (fixed spectral model), as described in Ren J. et al(27), was assumed, as previously done by Hu et al. and Xiaodong et al(19,28).

The signal fit was then optimized in Python (Python Software Foundation, Wilmington, Delaware, USA) using a Levenberg-Marquardt algorithm, as described by Xiaodong et al, where all unknowns (M_w, M_f, and R^*_{2eff}) are estimated for each voxel separately(19).

A second magnitude-based CSE algorithm (variable spectral model) was implemented by modifying the above reconstruction algorithm to include an additional fitting parameter, the susceptibility-induced shift of the water-fat frequency separation δ, to account for possible variations of the water-fat frequency difference:

$$C_n = \sum_{i=1}^{7} w_i e^{j(2\pi(\Delta f_i + \delta)TE_n)} \quad [3]$$

In this case, the parameters estimated by the first fixed spectra, a three-variable magnitude-based reconstruction algorithm, were used as initial values for the second Levenberg-Marquardt-based reconstruction algorithm to estimate FF and δ values.

Computation of microscopic susceptibility gradients and their effects on FF quantification accuracy

For all simulations, COMSOL Multiphysics software (COMSOL Inc., Palo Alto, California, USA) was used to compute the field distortion and frequency shift produced by magnetic susceptibility gradients for different microscopic water-fat distributions. These distributions included multiple cylindrical, droplet and layered geometries, as well as a few including different water-fat distributions within the same voxel (Figure 1). All simulations were computed assuming a static magnetic field B_o of 3T and a volume magnetic susceptibility of −9.04 ppm(29), in SI units, for water compartments, and −7.79 ppm for fat compartments(30). After solving the Maxwell equations in COMSOL, the sphere of Lorentz correction was applied(31), and the computed 3D magnetic vector field was exported to MATLAB (MathWorks, Inc., Natick, MA). The water and fat signal evolution was then computed from each spin for each simulated voxel and for several echo times: TE_n= [1.12, 2.34, 3.56, 4.78, 6.00, 7.39] ms, matching those used experimentally. Thae frequency distribution of water and fat spins, their relative difference, and the ratio of fat and water spins (true FF) was computed for each distribution by using the field map, assuming a T2* = 25 ms, and a macroscopic B_0-field inhomogeneity of 0 Hz(24). Signal magnitude and phase for each of the above echo times were fed into the two reconstruction algorithms to obtain a

FF values from the fixed ($\delta = 0$) and a variable δ spectral model, as well as the value of δ in field-independent units (ppm).

Phantom Experiment

In vitro experiments were performed on a Biograph mMR 3T (Siemens Healthcare, Germany). Samples consisted of a bovine meat sample containing layers of muscle, fat, and bone, and a 20% intralipid fat emulsion sample (Sigma-Aldrich, St. Louis, Missouri, USA). For all experiments, samples were equilibrated for 1.5 hours at bore temperature, measured by using a fiber optic temperature probe. 3D CSE FF measurements were performed along with single voxel spectroscopy (SVS) measurements, made at several locations within the sample. The samples were then rotated by 90° with respect to the B_0 field and CSE and MRS data were re-acquired.

For SVS measurements, a position resolved spectroscopy (PRESS) sequence was used with TE=30 ms, TR=2000 ms, 8mm × 8mm × 8mm voxel, 80 averages and without regional saturation bands. For the 3D CSE FF protocol, the following multi-echo gradient echo parameters were used: repetition time (TR), 15 ms; TE_n= [1.12 ms, 2.34 ms, 3.56 ms, 4.78 ms, 6.00 ms, 7.39 ms]; BW, 1180 Hz/Px; flip angle (FA), 3 degrees; field of view (FOV), 128mm × 128mm × 128mm; base resolution, 64; slices, 64; slice thickness, 2 mm; resolution, 2mm × 2mm × 2mm; readout mode, unipolar. The 1H spectra were fit in MATLAB by using pseudo-Voigt profiles. From each spectrum, the water-methylene resonance frequency shift was measured. Spectra with distorted lineshapes that could not be accurately fitted were excluded from the analysis. The 3D CSE imaging data were processed using the two reconstruction algorithms. Since all in vitro experiments were performed with a sample temperature of 24°C, a mean water-fat frequency separation of 3.53 ppm was used to account for the temperature-induced shift (−0.01ppm/°C) of the water resonance frequency.

In vivo Experiments

All human studies were approved by the Institutional Review Board and were conducted in compliance with the Helsinki Declaration and informed consent was obtained. For this study, CSE and CSI data acquired from 14 healthy volunteers were analyzed. Gender, age, and BMI of all participants are reported in Table 1.

The 3D CSE data in the supraclavicular region were acquired simultaneously with ^{18}F-FDG-PET maps in the same region as previously described in McCallister et al(10) in six young healthy volunteers, as well as in three overweight or obese middle-aged participants on a Biograph mMR (Siemens Healthcare, Germany) operating at a magnetic field of 3T. Specifically, a personalized cooling procedure was employed after 6 hours of fasting to maximally stimulate BAT non-shivering thermogenesis before (1 hour), and after (1 hour) injection of the ^{18}F-FDG radiotracer, injected at a reduced dose of 5 mCi. PET images in the supraclavicular area were acquired simultaneously with the 3D CSE data, which were acquired using a 1H chest coil strapped around the shoulders. For the 3D CSE acquisition a multi-echo gradient echo sequence was employed by using the following parameters: repetition time (TR), 15 ms; first echo time (TE), 1.12 ms; subsequent echo times (ΔTE),

1.22 ms; echoes, 6; FA, 3 degrees; BW, 1180 Hz/Px; FOV, 440mm × 225mm × 83mm; base resolution, 352; slices, 64; slice thickness, 1.3 mm; resolution, 1.3mm × 1.3mm × 1.3mm; readout mode, unipolar. The CSE data were fit using the two reconstruction algorithms using a water-fat frequency separation (water-methylene) of 3.4 ppm at 37°C(24).

Chemical shift imaging (CSI) and single voxel spectroscopy acquired on a PRISMA 3T scanner (Siemens Healthcare, Germany) in five volunteers, as part of a hyperpolarized 129Xe/1H spectroscopy study on human BAT, were retrospectively analyzed to quantify the mean separation between water and fat spins within the supraclavicular fat depot. All CSI data were acquired by using the following parameters: TR, 1.5 s; TE, 2.3 ms; bandwidth, 3 kHz; points, 2048; FOV, 400mm × 200mm; base resolution, 16 × 8; slices, 1; slice thickness, 2.5 mm; resolution, 2.5mm × 2.5mm × 2.5mm. From the spectrum of each CSI voxel containing supraclavicular fat tissue, the water-methylene resonance frequency shift was extracted. Again, spectra with distorted lineshapes or bimodal water and fat frequency distributions that could not be accurately fitted were excluded from the analysis.

Image Analysis

Fitting analysis was performed in Python (Python Software Foundation, DE). From the two reconstruction algorithms FF maps were obtained, with $FF=100*F/(F+W)$ for FF≥50% and $FF=100*(1-W/(F+W))$ for FF<50%. The difference in FF values obtained from the two reconstruction algorithms was calculated pixel by pixel. FF differences due to water fat swap were removed. Finally, from the second reconstruction algorithm, a map of the fitted parameter (δ) was created.

Statistical Analysis

Statistical analysis was performed in MATLAB. For significance testing two-tail t-tests were determined, and the level of significance was set at $p< 0.05$. The Bayesian Information Criterion (BIC) was calculated for both fits of each CSE image. A BIC difference of 6 between the two fits was taken as strong evidence of an improved spectral model(32).

Results

Figure 1.a shows all simulated geometries, a map of the shift δ induced by magnetic susceptibility gradients on the water-fat frequency separation (Fig. 1.b), and a plot of the water and fat frequency distributions ((Fig. 1.c). Table 2 shows the frequency shift induced by magnetic susceptibility gradients on the water and fat resonances. MFor the simulated geometries, this frequency shift varies from −0.4 ppm to 0.2 ppm. In addition, these simulations show, not only the relative water-fat distribution but also its orientation with respect to B_o matters. For example, for the infinite layers sample, a simple rotation of the sample with respect to the B_o field was able to induce a water-fat frequency shift as large as 0.6 ppm.

When not accounted for, these shifts can induce an error in the standard FF quantification as large as 18% when water-fat frequency shifts of 0.4 ppm are seen. In other geometries, the susceptibility-induced shift is on the order of 0.2 ppm, inducing a FF error on the order of 2–3%.

The reconstruction algorithm with a variable water-fat frequency separation was able to correctly quantify the average water-fat frequency separation computed from the field map within 0.011 ppm and estimate the true FF with an error of less than 1%, compared to an average error of 4.5% of the reconstruction algorithm with the fixed water-fat frequency separation. However, when the distribution of water and fat spins gave rise to a bimodal frequency distribution for one or both spin species, errors as large as 3% were seen, even when a spectral model with a variable water-fat frequency separation was employed. In these cases, accounting for a susceptibility-induced frequency shift was not enough to correctly quantify FF.

Figure 2 shows gradient echo images and an example of one of the many voxels selected for spectroscopic measurements of the water-fat frequency separation for the meat and intralipid solution samples, for two orthogonal orientations with respect to the B_o field. The figure also shows the average water-fat frequency difference measured across the two samples, by SVS, for the two orientations. The mean value and the standard deviation of the water-fat frequency separation for the meat sample were: 3.75±0.15 ppm, when the muscle and fat layers were oriented orthogonal to the B_o field; 3.59±0.04 ppm, when the muscle and fat layers were oriented parallel the B_o field (P=0.049); 3.67±0.04 ppm, when both orientations were considered. Although the mean difference in water-fat frequency separation between the two orientations was 0.2 ppm, across the entire sample the difference was measured to be as large as 0.42 ppm. For the intralipid solution, the mean water-methylene frequency separations and standard deviations were: 3.57±0.03 ppm for parallel position; 3.61±0.13 ppm for a position perpendicular to the B_o field; (P=0.099) 3.59±0.01 ppm for the combined positions. In this case, a rotation of the sample with respect to the main field B_o did not produce an appreciable change in the water-fat frequency difference.

Figure 3 shows a map of δ as obtained by using the second reconstruction algorithm across the entire meat sample for the two orientations of the samples and for the combined orientations. When the muscle-fat layers are oriented along the main field B_o, the largest susceptibility-induced frequency shift ($\delta = \pm 0.7$ ppm) is seen at water-fat boundaries. In agreement with the simulated results, a larger susceptibility-induced frequency shift ($\delta = \pm 1$ ppm) is seen when the muscle-fat layers are oriented perpendicular to the direction of the main field B_o.

Figure 4 shows FF maps obtained with the two reconstruction algorithms for the two orientations of the meat sample. Larger differences in FF on the order of 5% are seen predominately at the interfaces between the muscle and fat layers. Different values are obtained also within the muscle and fat layers when the sample is oriented orthogonal to the direction of B_o.

Figure 5 shows the relationship between the absolute differences in FF values obtained by using the two reconstruction algorithms and the susceptibility-induced frequency shift δ for the two orientations of the meat sample. FF difference increases sharply with δ, with a FF difference of 3% being caused by a delta of 0.3 ppm. This dependence levels out, with a small increase in FF difference for $\delta > 0.3$ ppm.

Figure 6 shows a ^{18}F-FDG-PET image of the supraclavicular region from one of the subjects (subject 5) analyzed in this study, along with FF maps of the same area as obtained by the two magnitude-based CSE reconstruction algorithms. Although the mean supraclavicular FF measured with the two spectral models was quite similar, 70% for the spectral model with a fixed water-fat frequency separation and 69% for the spectral model with a variable water-fat frequency separation, with a mean difference of 0.8% FF and a standard deviation of 2.8%, the difference in FF for the individual voxel was on the order of 5%. These differences in FF were caused by a water-fat frequency separation that, for some voxels, deviated from the nominal 3.4 ppm by as much as 0.5 ppm. When the goodness of the individual fit models was examined voxel by voxel by using the BIC, 88% of voxels within the supraclavicular fat depot showed that the second reconstruction algorithm, the one that accounted for a susceptibility-induced water-fat frequency shift δ, was significantly better (difference in BIC > 6) than the first reconstruction algorithm, which didn't account for a variability in the water-fat frequency separation.

Figure 7 shows the same map for the entire region in the same subject. Interestingly, in muscle the two reconstruction algorithms show even larger δ values and FF differences. The second algorithm shows a systematically higher FF of up to 11%, which is greater than the difference shown in supraclavicular fat. However, unlike in the supraclavicular fat region, when the goodness of the individual fit models was examined voxel by voxel by using the BIC, the majority of the voxels (78%) showed no improvement with the variable spectral model (difference in BIC < 2).

Figure 8 shows boxplots of the range of the difference in FF values obtained by the two reconstruction algorithms, and the range of δ values obtained from the second algorithm, as measured in the supraclavicular fat of all 9 participants (6 lean and 3 obese) that underwent the CSE protocol. In all subjects, the two reconstruction algorithms produced similar supraclavicular mean FF values. Differences in FF between the in lean subjects was −1% ±5% and −1%±3% in obese subjects. While in all lean subjects the presence of BAT in the supraclavicular fat depot was confirmed by an increase in glucose uptake in the PET scan, in the 3 obese subjects glucose uptake was below the nominal detection threshold of SUV=1.5 and the presence of BAT could not be confirmed.

Among all lean subjects, in subject 3, differences in FF were slightly larger. This subject had supraclavicular fat with the lowest FF with a mean value close to 62%. The average water-fat frequency separation in the supraclavicular region for all lean subjects was 3.49±0.15 ppm (δ = 0.09±0.15 ppm), with values ranging from 3 ppm (δ = −0.4 ppm) to 4 ppm (δ = 0.6 ppm). In obese, older subjects, the average water-fat frequency separation was seen to be 3.41±0.16 ppm (δ = 0.01±0.16 ppm).

Figure 8 also shows a Blandt-Aldman plot of every voxel analyzed in the supraclavicular fat region for all 6 lean subjects. The difference in FF values obtained from the two reconstruction algorithms is plotted against the average of the two FF values. The two reconstruction algorithms produced similar FF values for most of the voxels, with a mean difference in FF of 1.2% and a standard deviation of 5.26%. However, for some of the voxels, especially those with a FF ranging between 40% and 60%, differences in FF ranged

from −25% to 15%. Figure 8.d reports boxplots of the susceptibility-induced water-fat frequency shift δ as obtained from the 5 subjects that underwent the CSI scans. Across all five subjects the water-fat frequency separation had a mean of 3.44±0.16 ppm and ranged from 3.1 to 3.8 ppm, nicely matching the values obtained by using the second CSE reconstruction algorithm that accounted for the susceptibility-induced water-fat frequency shift δ.

Discussion

Unlike the effect of macroscopic field inhomogeneities, which are often accounted for in CSE FF quantification reconstruction algorithms, the effect of microscopic susceptibility gradients on CSE FF quantification, aside from fat infiltration in skeletal muscle(25), has been left largely unexplored. Here we show that, in the supraclavicular region, where BAT is located, the shift produced by microscopic susceptibility gradients on the water-fat frequency separation are on average 0.1 ppm with a standard deviation of 0.2 ppm, but with individual values ranging from a minimum of −0.3 ppm to a maximum of 0.6 ppm. The magnitude of these shifts is consistent with the magnitude of the water-fat frequency shift generated by microscopic susceptibility gradients and computed in this study. This is not surprising as the supraclavicular tissue, at the microscopic level, is highly heterogeneous, with nerves, brown fat, white fat, and blood vessels that often are not resolved in MR images. Further confirmation of the validity of these values comes from CSI analysis of supraclavicular fat, where the measured water-fat frequency shifts ranged from −0.3 ppm to 0.4 ppm. These susceptibility-induced frequency shifts are equivalent to the frequency shifts induced by a change in temperature from +30°C to −40°C, thus much larger that the small temperature-induced shift of few hundredths of a ppm that can be expected from activation of BAT in humans.

Our data also shows that the mean water-fat frequency separation in supraclavicular fat tissue is around 3.5 ppm, higher than the 3.4 ppm water-fat separation often used for FF quantification(20). This is not surprising, as the 3.4 ppm value was originally measured in human liver, where the microscopic distribution of water and fat spins is expected to be different than in the supraclavicular fat. As shown by our simulation and in vitro experiments, the water-fat separation strongly depends on the specific microscopic distribution of water and fat spins and on its orientation with respect to B_o.

Our simulations also show that these susceptibility-induced frequency shifts can produced FF errors as large as 18%, when not accounted for, and much smaller errors, on the order of 0.4%, when susceptibility-induced water-fat frequency shifts are included in the spectral model. Differences in FF between the two models ranged from less than 1% when the frequency shift was small (~0.1 ppm) up to 18% when the frequency shift was large (~0.4 ppm).

The CSE and CSI results in the phantoms mimicked these results showing large differences in the water fat frequency separation upon rotation in the field in the inhomogeneous, layered bovine phantom, while very little shift was observed in the homogenous droplet-like emulsion. Theoretically, these shifts have a possible range of 1.25 ppm, depending on the

microscopic geometries, however in simulations and in phantom experiments a maximum deviation of 0.4 was found to be realistic(33). Although not directly comparable to CSE due to difference in voxel size, the retrospective CSI data showed the existence of these large shifts also in vivo, in the supraclavicular fat depot. In the supraclavicular fat depot, the two CSE models gave rise to similar frequency shifts and FF differences, with a mean absolute difference in FF of 1% and a standard deviation of 5% in lean subjects. Obese subjects showed the same mean shift with a smaller standard deviation of 3%. The smaller deviation in FF in obese subjects is possibly due to a reduction or lack of BAT in the region. In both obese and lean subjects, some individual voxels showed differences up to 25%. However, these larger differences should be interpreted with care since, in vivo, the true FF value is not known, and the difference could be due to noise and/or to a model break-down. Both models assume a uniform distribution for both water and fat spins. However, as seen in the simulations, when the frequency distribution of one or both spin species is multimodal, both models fail to correctly describe the underlying signal, possibly giving rise to large FF errors. The variable spectral model does not correct for all biases such as these multimodal distributions, or for chemical shift displacement artifacts, however it should minimize biases in inhomogeneous fatty tissues.

An analysis of the goodness of the model suggests that in the supraclavicular fat depot, where BAT is located and FF ranges from 40% to about 70%, the variable model, that accounts for susceptibility-induced frequency shifts, does a much better job in describing the underlying signal in lean subjects (mean difference in BIC of 11.0±0.4). In obese subjects, it still does a better job, however differences are less pronounced and a larger spread of values are observed (mean difference in BIC of 4±6). However, in the muscle tissue, where FF is considerably low and tissue is more homogenous, that is no longer the case. In this case, the problem seems to be ill-conditioned in the presence of noise; if one of the species is present at much lower concentrations, it is harder to estimate the frequency separation between the two spins. In this case, the second model that accounts for the susceptibility-induced frequency shift, by introducing an additional degree of freedom, may actually degrade model performance (mean difference in BIC of 1±4). In this case, a possible solution could be the use of a constrained reconstruction algorithm at the expense of increased complexity.

It is important to note that, on many clinical applications, in which mean FFs are taken across a relatively large ROI, an error in tissue FF of 1±5% may not seem to be significant. However, when looking at small changes in tissue fat fractions, as those expected in BAT during stimulation of thermogenesis, an error of 5% can make the results unreliable(12). Such errors could explain the contrasting results obtained in humans BAT when measuring changes in tissue fat fraction during cold exposure by FF techniques.

There are several limitations to this study. First, a FF ground truth for the meat phantom and for the supraclavicular tissue was not available. Therefore, we were able to analyze only differences in FF values provided by the two CSE models and use the BIC to determine the relative goodness of the two spectral models. Second, because of the large difference in resolution between SVS and CSE methods, the two methods could not be directly compared. Also, because a PRESS sequence was used, only the average water-fat frequency separation could be estimated using the SVS method.

In conclusion, in inhomogeneous fatty tissues, like the supraclavicular fat depot, microscopic magnetic susceptibility gradients induce a shift of the water-fat frequency separation by as much as ±0.4 ppm. This shift can lead to errors in estimations of tissue fat fraction in individual voxels on the order of 5%. Since the magnitude of the shift strongly depends on the microscopic distribution of water and fat spins within the image voxel, as well as on its orientation with respect to B_0, its value is expected to vary from voxel to voxel. This can be minimized in fatty tissues by using a reconstruction algorithm that employs a spectral model with a variable water-fat frequency separation. While this effect is small enough to be negligible in many clinical and research applications, this effect could be significant in the case of detection of BAT lipid consumption by fat fraction MR techniques.

Acknowledgments

Grant Support: This work was funded by the National Institutes of Health, through Grant Award R01DK108231.

References

1. van Marken Lichtenbelt W, Vanhommerig J, Smulders N, Drossearts J, Kemerink G, Bouvy N, et al. Cold-Activated Brown Adipose Tissue in Healthy Men. N Engl J Med. 2009; 360(15):1500–8. [PubMed: 19357405]
2. Gunawardana SC, Piston DW. Reversal of type 1 diabetes in mice by brown adipose tissue transplant. Diabetes. 2012; 61(3):674–82. [PubMed: 22315305]
3. Seale P, Lazar Ma. Brown fat in humans: Turning up the heat on obesity. Diabetes. 2009; 58(7): 1482–4. [PubMed: 19564460]
4. Lowell BB, S-Susulic V, Hamann A, Lawitts Ja, Himms-Hagen J, Boyer BB, et al. Development of obesity in transgenic mice after genetic ablation of brown adipose tissue. Nature. 1993; 366(6457): 740–2. [PubMed: 8264795]
5. Cypess AM, Haft CR, Laughlin MR, Hu HH. Brown fat in humans: consensus points and experimental guidelines. Cell Metab. 2014; 20(3):408–15. [PubMed: 25185947]
6. Sampath SC, Sampath SC, Bredella MA, Cypess AM, Torriani M. Imaging of Brown Adipose Tissue: State of the Art. Radiology. 2016; 280(1):4–19. [PubMed: 27322970]
7. Hu HH, Smith DL, Nayak KS, Goran MI, Nagy TR. Identification of brown adipose tissue in mice with fat-water IDEAL-MRI. J Magn Reson Imaging. 2010; 31(5):1195–202. [PubMed: 20432356]
8. Gifford A, Walker RC, Towse TF, Brian Welch E. Correlations between quantitative fat-water magnetic resonance imaging and computed tomography in human subcutaneous white adipose tissue. J Med imaging (Bellingham, Wash). 2015; 2(4):46001.
9. van Rooijen BD, van der Lans AaJJ, Brans B, Wildberger JE, Mottaghy FM, Schrauwen P, et al. Imaging Cold-Activated Brown Adipose Tissue Using Dynamic T2*-Weighted Magnetic Resonance Imaging and 2-Deoxy-2-[18F]fluoro-D-glucose Positron Emission Tomography. Invest Radiol. 2013; 48(10):1–7. [PubMed: 23070097]
10. McCallister A, Zhang L, Burant A, Katz L, Branca RT. A pilot study on the correlation between fat fraction values and glucose uptake values in supraclavicular fat by simultaneous PET/MRI. Magn Reson Med. 2017; 0
11. Bauwens M, Wierts R, Van Royen B, Bucerius J, Backes W, Mottaghy F, et al. Molecular imaging of brown adipose tissue in health and disease. Eur J Nucl Med Mol Imaging. 2014; 41(4):776–91. [PubMed: 24509875]
12. Lundström E, Strand R, Johansson L, Bergsten P, Ahlström H, Kullberg J. Magnetic Resonance Imaging Cooling-Reheating Protocol Indicates Decreased Fat Fraction via Lipid Consumption in Suspected Brown Adipose Tissue. PLoS One. 2015; 10(4):e0126705. [PubMed: 25928226]
13. Stahl V, Maier F, Freitag MT, Floca RO, Berger MC, Umathum R, et al. In vivo assessment of cold stimulation effects on the fat fraction of brown adipose tissue using DIXON MRI. J Magn Reson Imaging. 2016:369–80. [PubMed: 27421080]

14. Reeder SB, Robson PM, Yu H, Shimakawa A, Hines CDG, McKenzie CA, et al. Quantification of hepatic steatosis with MRI: The effects of accurate fat spectral modeling. J Magn Reson Imaging. 2009; 29(6):1332–9. [PubMed: 19472390]
15. Ma X, Holalkere N-S, R AK, Mino-Kenudson M, Hahn PF, Sahani DV. Imaging-based Quantification of Hepatic Fat: Methods and Clinical Applications1. RadioGraphics. 2009; 29(5): 1253–77. [PubMed: 19755595]
16. Kühn JP, Hernando D, Mensel B, Krüger PC, Ittermann T, Mayerle J, et al. Quantitative chemical shift-encoded MRI is an accurate method to quantify hepatic steatosis. J Magn Reson Imaging. 2014; 39(6):1494–501. [PubMed: 24123655]
17. Wang X, Hernando D, Reeder SB. Sensitivity of chemical shift-encoded fat quantification to calibration of fat MR spectrum. Magn Reson Med. 2016; 75(2):845–51. [PubMed: 25845713]
18. Yu H, Shimakawa A, Hines CDG, McKenzie CA, Hamilton G, Sirlin CB, et al. Combination of complex-based and magnitude-based multiecho water-fat separation for accurate quantification of fat-fraction. Magn Reson Med. 2011; 66(1):199–206. [PubMed: 21695724]
19. Zhong X, Nickel MD, Kannengiesser SAR, Dale BM, Kiefer B, Bashir MR. Liver fat quantification using a multi-step adaptive fitting approach with multi-echo GRE imaging. Magn Reson Med. 2014; 72(5):1353–65. [PubMed: 24323332]
20. Wang X, Hernando D, Reeder SB. Sensitivity of Chemical Shift-Encoded Fat Quantification to Calibration of Fat MR Spectrum. Magn Reson Med. 2016; 75(2):845–51. [PubMed: 25845713]
21. Yu H, Shimakawa A, Mckenzie Ca, Brodsky E, Brittain JH, Reeder SB. Multi-Echo Water-Fat Separation and Simultaneous R2* Estimation with Multi-Frequency Fat Spectrum Modeling Huanzhou. Magn Reson Med. 2008; 60(5):1122–34. [PubMed: 18956464]
22. Hernando D, Kellman P, Haldar JP, Liang ZP. Robust water/fat separation in the presence of large field inhomogeneities using a graph cut algorithm. Magn Reson Med. 2010; 63(1):79–90. [PubMed: 19859956]
23. Hindman JC. Proton Resonance Shift of Water in the Gas and Liquid States. J Chem Phys. 1966; 44(12):4582.
24. Hernando D, Sharma SD, Kramer H, Reeder SB. On the confounding effect of temperature on chemical shift-encoded fat quantification. Magn Reson Med. 2014; 72(2):464–70. [PubMed: 24123362]
25. Karampinos DC, Yu H, Shimakawa A, Link TM, Majumdar S. Chemical shift-based water/fat separation in the presence of susceptibility-induced fat resonance shift. Magn Reson Med. 2012; 68(5):1495–505. [PubMed: 22247024]
26. Hong CW, Mamidipalli A, Hooker JC, Hamilton G, Wolfson T, Fazeli S, et al. Robust agreement between MRI and MRS hepatic proton density fat fraction despite biologically plausible variability in fat spectra in patients with nonalcoholic steatohepatitus. ISMRM. 2017:362.
27. Ren J, Dimitrov I, Sherry DA, Malloy CR. Composition of Adipose Tissue and Marrow Fat by 1H MR Spectroscopy at 7 Tesla. J Lipid Res. 2008; 49:2055–62. [PubMed: 18509197]
28. Hu HH, Perkins TG, Chia JM, Gilsanz V. Characterization of Human Brown Adipose Tissue by Chemical-Shift Water-Fat MRI. AJR Am J Roentgenol. 2013; 200(1):177–83. [PubMed: 23255760]
29. Poorter J, De Wagter C, De Deene Y, De Thomsen C, Stalhlberg F, Achten E. Noninvasive MRI Thermometry with the Proton Resonance Frequency (PRF) Method: In Vivo Results in Human Muscle. Magn Reson Med. 1995; 33(1):74–81. [PubMed: 7891538]
30. Hopkins JA, Wehrli FW. Magnetic susceptibility measurement of insoluble solids by NMR: Magnetic susceptibility of bone. Magn Reson Med. 1997; 37(4):494–500. [PubMed: 9094070]
31. Durrant CJ, Hertzberg MP, Kuchel PW. Magnetic susceptibility: Further insights into macroscopic and microscopic fields and the sphere of Lorentz. Concepts Magn Reson Part A Bridg Educ Res. 2003; 18(1):72–95.
32. Raftery AE. Bayes factors and BIC. Sociol Methods Res. 1999; 27(3):411–27.
33. Chu SCK, Xu Y, Balschi JA, Springer CS. Bulk magnetic-susceptibility shifts in NMR-studies of compartmentalized samples - use of paramagnetic reagents. Magn Reson Med. 1990; 13(2):239–62. [PubMed: 2156125]

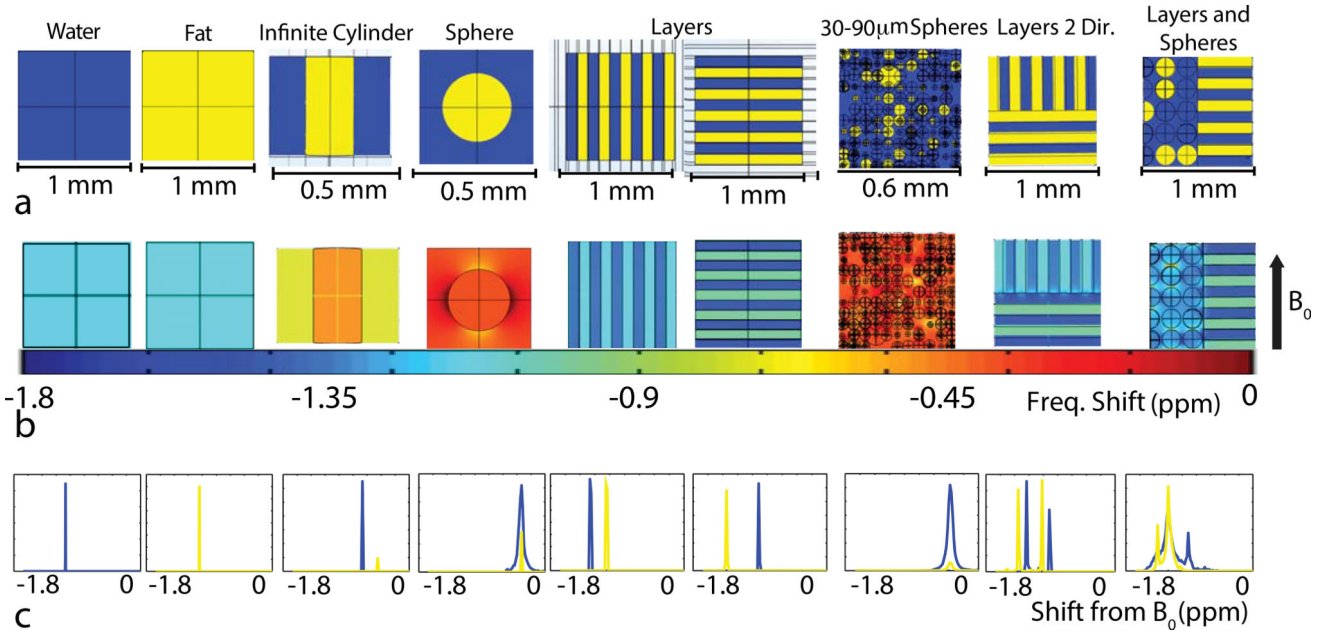

Figure 1.

a. Cartoon of simulated water (blue) and fat (yellow) distributions. Please note the small scale used to analyze the effect of intra-voxel susceptibility gradients b. Map of the magnetic susceptibility-induced frequency shift for the above distributions. c. Histograms of the water (blue) and fat (yellow) frequency distributions for the simulated voxel.

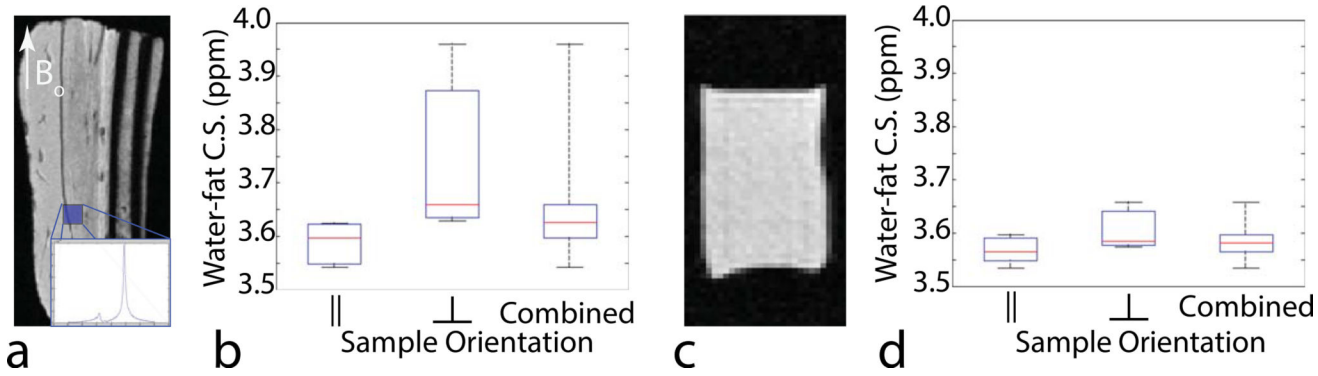

Figure 2.

a. Coronal slice of a 3D gradient echo data set of the meat sample, sketching the location of one of the spectroscopy voxels and the direction of B_o for the fat layers aligned parallel to B_o. b. Box plot of the water-methylene frequency separation obtained from N=5 SVS spectra acquired on the meat sample oriented with the fat layers aligned parallel to the direction of B_o, orthogonal to the direction of B_o, and for the combined alignments. c. Axial slice of the first echo image of the intralipid phantom illustrating the geometry. d. Boxplot of the water-methylene frequency separation obtained from N=5 SVS spectra taken with the main axis of the centrifuge tube aligned parallel and perpendicular to the main magnetic field, and for the combined sample orientations.

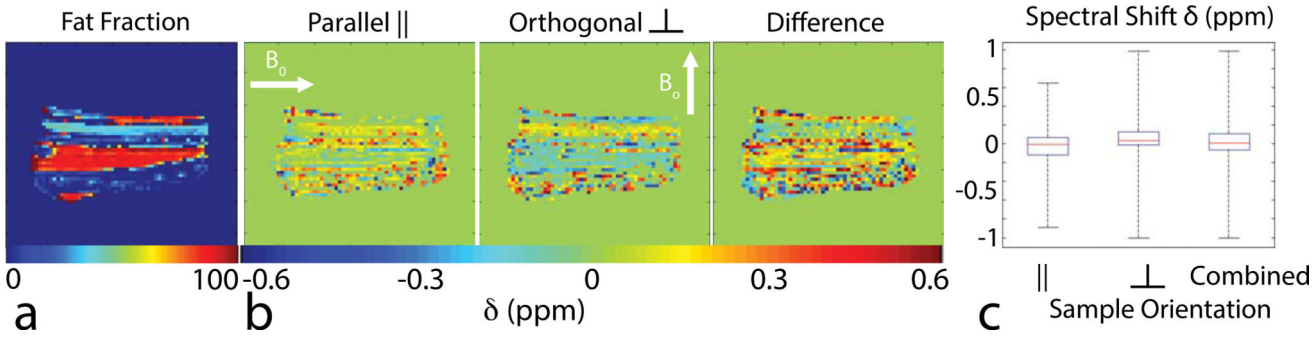

Figure 3.

a. FF map obtained using the reconstruction algorithm with the fixed water-fat separation. b. 2D maps and box-lot of the susceptibility-induced water-fat frequency shift (δ) for different orientations of the meat sample. c. Boxplots of the susceptibility-induced water-fat frequency shift (δ) for both orientations and the two orientations combined. The mean susceptibility-induced frequency shift δ and standard deviations were: orthogonal, −0.01±0.19 ppm, parallel 0.05±0.17 ppm, (p<0.001), combined 0.02±0.18 ppm.

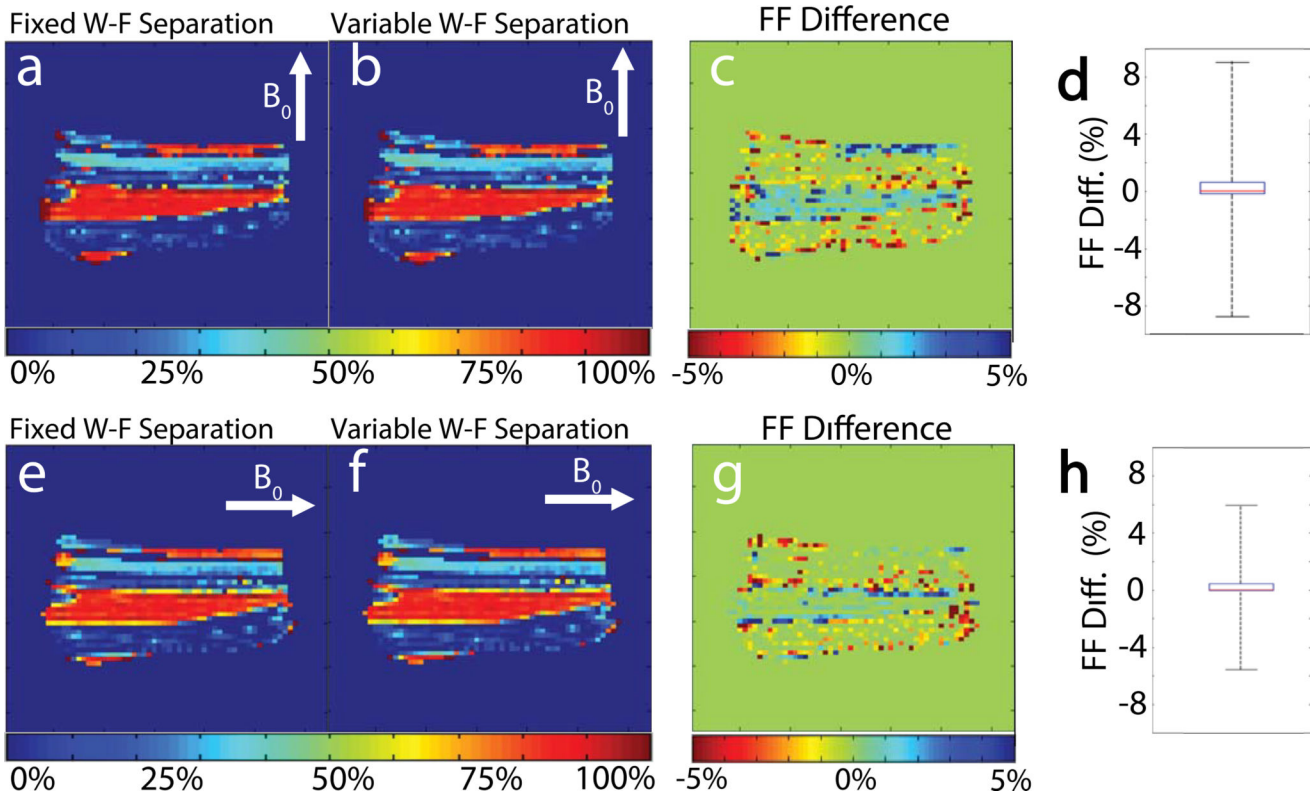

Figure 4.

a–b FF map of the meat phantom with the fat layers oriented orthogonally to the B_0 field as obtained with the two algorithms: magnitude-based algorithms with a fixed (a) water-fat frequency separation and a variable (b) water-fat frequency separation. c. Difference map between the two reconstruction algorithms. d. Boxplot of the difference in FF values. Mean FF difference and standard deviation: 0.48±2.98%. e-f. FF map of the meat phantom with the fat layers oriented parallel to the B_0 field as obtained with the magnitude-based reconstruction algorithms with a fixed (e) and a variable (f) water-fat frequency separation. g. Difference map between the two reconstruction algorithms. h. Boxplot of the difference in FF values. Mean FF difference and standard deviation: 0.22±2.88%. For the two orientations, the distributions of the difference in FF values showed significant differences using a two-sample t-test (P<0.03).

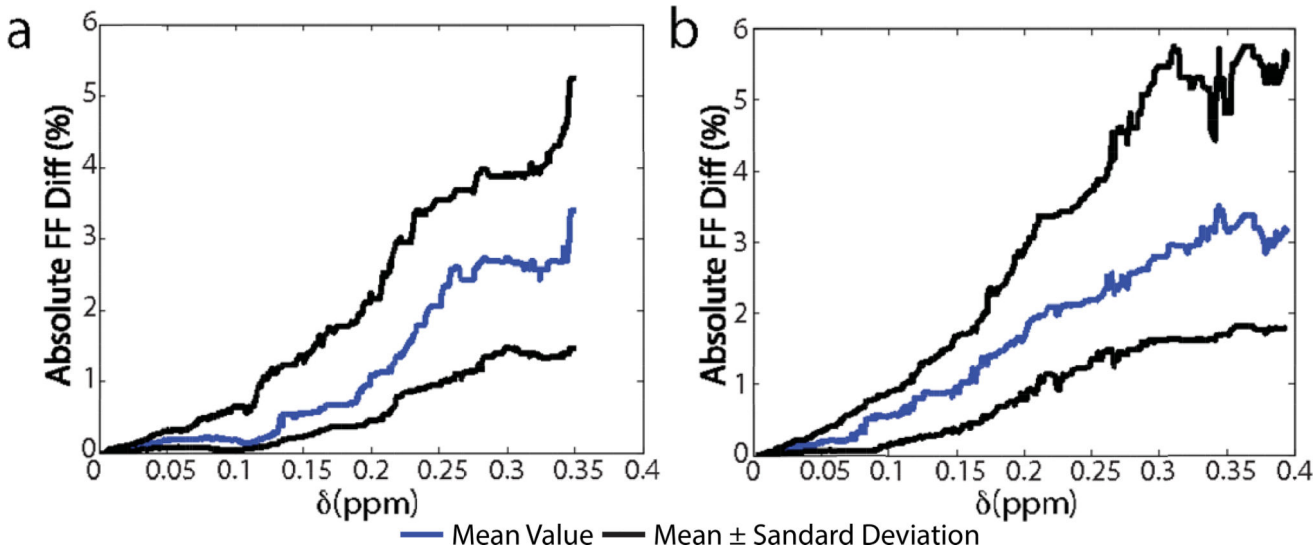

Figure 5.

a–b Plot of the difference in FF values obtained from the two reconstruction algorithms as a function of the susceptibility-induced frequency shift δ for the meat sample in the (a) orthogonal and (b) parallel orientation. Individual voxels were ordered based on FF difference and 15 voxels on either side were interpolated over to determine the mean water-fat frequency separation and standard deviation for each FF difference. The blue line shows the mean frequency shift while the black lines shows the mean FF ± the standard deviation.

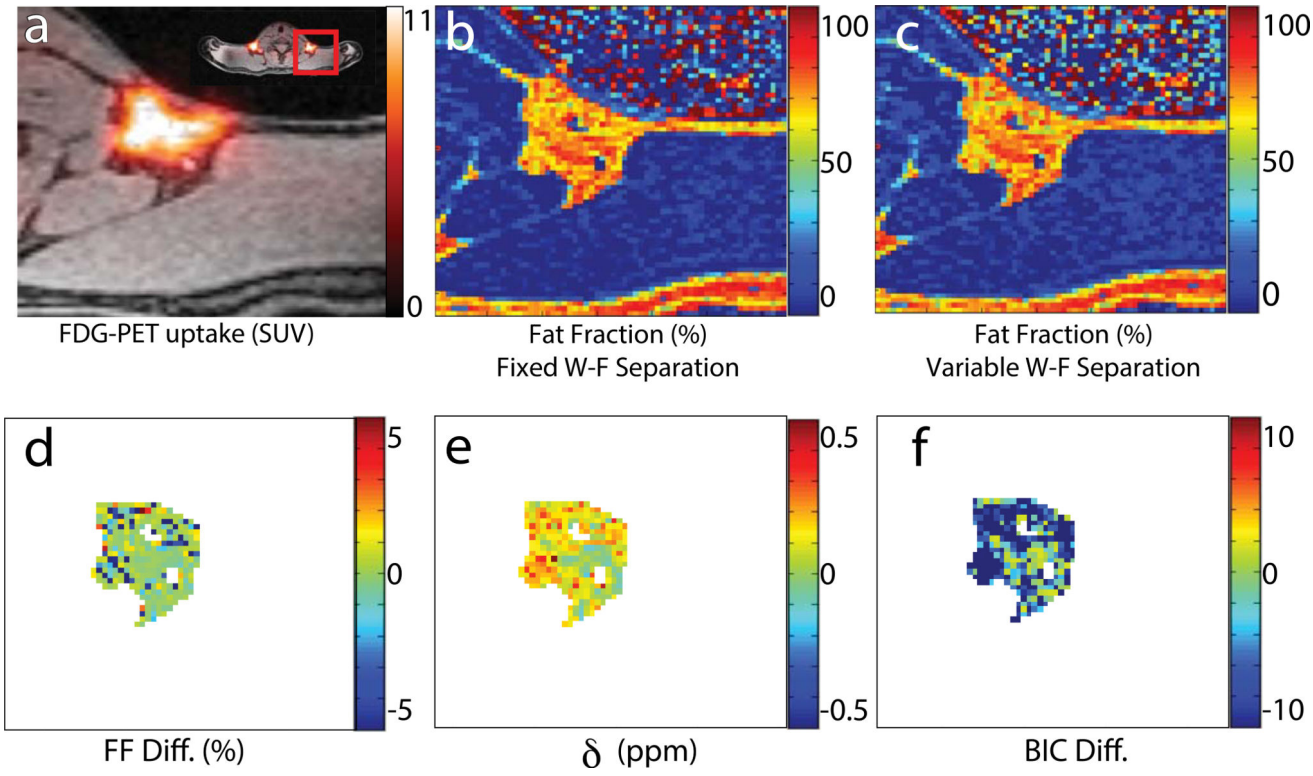

Figure 6.

a. Axial slice from Subject 5 of both the MR and ^{18}F-FDG-PET image (23 y.o. female with a BMI of 21) highlighting the glucose avid supraclavicular region. The red square indicates the region of interest analyzed. Significant ^{18}F-FDG-uptake can be seen in the same region analyzed. b. FF map of the highlighted region as obtained by using the first magnitude-based reconstruction algorithm. c. FF map of the same region as obtained by using the second reconstruction algorithm that accounts for the susceptibility-induced water-fat frequency shift. For this subject, the mean difference in FF between the two reconstruction algorithms was −0.8%, with a standard deviation of 2.8%. d. Difference map masked at 40% FF to highlight the supraclavicular fat depot. e. Masked map of the susceptibility-induced frequency shift δ as obtained from the second reconstruction algorithm. f. Masked map of the difference in BIC values between the two reconstruction algorithms ($BIC_{variable}$-BIC_{fixed}).

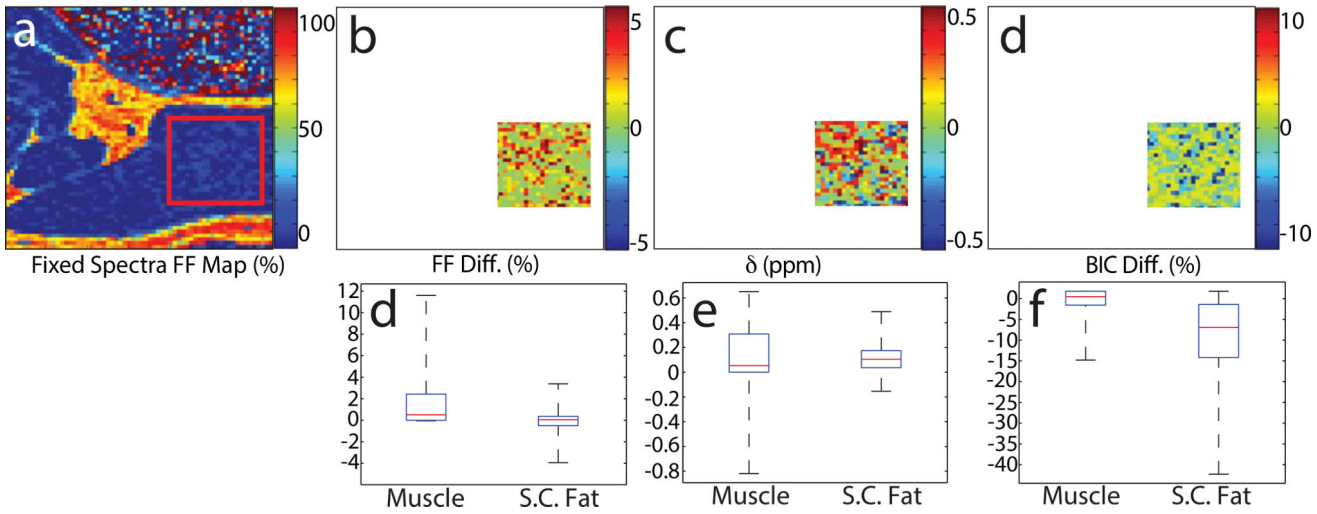

Figure 7.

a. FF map of the supraclavicular region of Subject 5 (23 y.o. female with a BMI of 21). The red square indicates the region analyzed as muscular tissue. Supraclavicular fat is defined as the masked region in Figure 6. b. Full un-masked FF difference map. c. Full un-masked map of the susceptibility-induced water-fat frequency shift δ as obtained from the second reconstruction algorithm. d. Full un-masked map of the difference in BIC values between the two reconstruction algorithms ($BIC_{variable}$-BIC_{fixed}). e. Box plot of the FF difference seen in muscle (1.4±1.8%) and supraclavicular fat (−0.8±2.8%) f. Box plot of the susceptibility-induced water-fat frequency shift δ in muscle (0.11±0.23 ppm) and supraclavicular fat (0.11±0.10 ppm). g. Box plot of the BIC difference in muscle (0.7±3.5) and supraclavicular fat (−8.8±8.8 ppm).

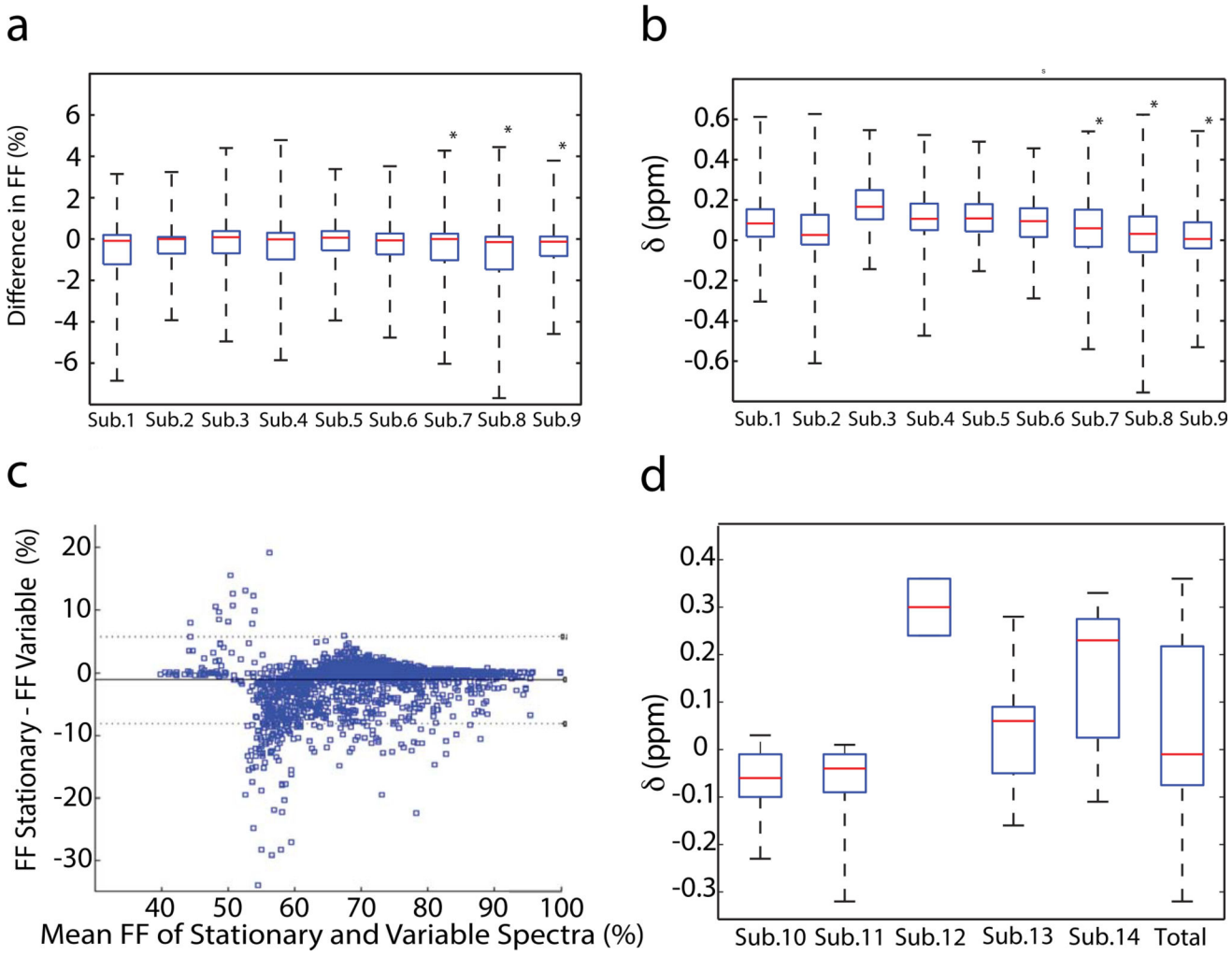

Figure 8.

a. Boxplot of the difference in FF values measured with the two reconstruction algorithms for the supraclavicular fat depot of all 9 subjects. Mean and standard deviation of the difference in FF obtained with the two algorithms: Subject 1: 1±4%; Subject 2: 2±8%; Subject 3: 1±6%; Subject: 4 1±4%; Subject 5: 1±3%; Subject 6: 1±3%; Subject 7: 1±4%; Subject 8: 1±3%; Subject 9: 1±4%. b. Boxplot of the susceptibility-induced water-fat frequency shift δ for all 9 subjects. Mean and standard deviation values are: Subject 1: 0.1±0.1 ppm; Subject 2: 0.0±0.2 ppm; Subject 3: 0.1±0.1 ppm; Subject 4: 0.1±0.1 ppm; Subject 5: 0.1±0.1 ppm; Subject 6: 0.1±0.1 ppm; Subject 7: 0.1±0.2 ppm; Subject 8: 0.0±0.2 ppm; Subject 9: 0.0±0.2 ppm. c. Bland-Altman plot of the two magnitude-based reconstruction algorithms for all 6 lean subjects from an axial slice encompassing the supraclavicular region and masked with a 40% FF. d. Boxplot of the susceptibility-induced water-fat frequency shift δ as measured by CSI in the supraclavicular fat region for five subjects. Values are displayed relative to the nominal value of 3.4 ppm. When combined, the mean difference in separation was 0.04±0.16 ppm, with a range from −0.3 to 0.4 ppm. * denotes overweight or obese subjects

Table 1

Sex, Age and BMI of the subjects scanned.

Subject	Sex	Age	BMI
1*	F	27	23.7
2*	M	23	24.4
3*	M	22	22.2
4*	F	24	24.3
5*	F	23	21.0
6*	M	21	23.4
7*	F	38	29.4+
8*	M	43	36.6+
9*	F	49	34.2+
10**	F	31	22.5
11**	F	31	22.5
12**	F	26	22.3
13**	F	26	22.3
14**	F	31	24.8

* denotes subjects scanned on Biograph PET/MR 3T

** denotes subjects scanned on PRISMA 3T.

+ denotes overweight or obese subjects.

Table 2

Results of the B-field simulations of the water and fat frequency distribution. From the water and fat frequency distribution, average water frequency shift, average fat frequency shift, and average water-fat frequency separation were calculated. The true FF value was the one used in the simulations. The estimated δ, was the one computed by the variable spectra fit. FF and variable FF were taken from the fixed spectra fit (δ = 0) and variable spectra fit, respectively.

Geometry	Water Shift (ppm)	Fat Shift (ppm)	Water-Fat Susceptibility induced Shift (ppm)	True FF (%)	Estimated δ (ppm)	FF $\delta = 0$ (%)	FF Variable δ (%)
Water	1.067	N/A	N/A	0.00	N/A	0.00	N/A
Fat	N/A	1.042	N/A	100.00	N/A	99.92	N/A
Vertical Infinite Cylinder	0.672	0.455	0.217	13.39	0.217	12.80	13.39
Horizontal Infinite Cylinder	0.668	0.751	−0.083	14.20	−0.096	13.25	14.52
Infinite Vertical Layers	1.259	1.042	0.217	50.00	0.217	48.03	49.97
Infinite Horizontal Layers	0.914	1.348	−0.434	50.00	−0.434	32.46	50.00
30 um fat sphere	0.335	0.335	0	8.03	−0.010	8.37	8.42
Fat spheres 30um to 90um in random distribution	0.350	0.349	0.001	18.41	−0.007	18.78	18.82
Vertical and Horizontal Layers	1.090	1.194	−0.104	53.08	−0.107	50.34	52.94
Vertical Layers and fat spheres	1.140	1.122	0.018	37.92	0.053	39.55	39.37
Horizontal Layers and fat spheres	1.158	1.214	−0.055	37.92	−0.037	38.95	39.22